Geophysical Research Letters

RESEARCH LETTER
10.1029/2022GL099475

Special Section:
Results from Juno's Flyby of Ganymede

Gravity Field of Ganymede After the *Juno* Extended Mission

L. Gomez Casajus[1], A. I. Ermakov[2], M. Zannoni[1,3], J. T. Keane[4], D. Stevenson[5], D. R. Buccino[4], D. Durante[6], M. Parisi[4], R. S. Park[4], P. Tortora[1,3], and S. J. Bolton[7]

[1]Interdepartmental Center for Industrial Research in Aerospace (CIRI AERO), Alma Mater Studiorum – Università di Bologna, Forlì, Italy, [2]Space Sciences Laboratory, University of California, Berkeley, CA, USA, [3]Department of Industrial Engineering, Alma Mater Studiorum – Università di Bologna, Forlì, Italy, [4]Jet Propulsion Laboratory, California Institute of Technology, Pasadena, CA, USA, [5]Division of Geological and Planetary Sciences, California Institute of Technology, Pasadena, CA, USA, [6]Department of Mechanical and Aerospace Engineering, Sapienza University of Rome, Rome, Italy, [7]Southwest Research Institute, San Antonio, TX, USA

Abstract The *Juno* Extended Mission presented the first opportunity to acquire gravity measurements of Ganymede since the end of the *Galileo* mission. These new *Juno* data offered the chance to carry out a joint analysis with the *Galileo* data set, improving our knowledge of Ganymede's gravity field and shedding new light upon its interior structure. Through reconstruction of *Juno*'s and *Galileo*'s orbit during the Ganymede flybys, the gravity field of the moon was estimated. The results indicate that Ganymede's degree-2 field is compatible with a body in hydrostatic equilibrium within $1-\sigma$ and hint at regional gravity anomalies with amplitudes exceeding those inferred by *Cassini* for Titan. Our explicit treatment of non-hydrostatic effects leads to wider confidence intervals for the derived moment of inertia with respect previous analyses. The higher central value of the derived moment of inertia indicates a lesser degree of Ganymede's differentiation.

Plain Language Summary On 7 June 2021, *Juno* performed the first close flyby of Ganymede, the largest satellite of Jupiter (and the largest moon in the Solar System), since the end of the *Galileo* mission. The gravity field of Ganymede was reconstructed using the radio tracking data from all of the Ganymede encounters of both the *Galileo* and *Juno* missions. The data analysis hints at localized gravity anomalies. Interpretation of the gravity data suggests a slightly higher moment of inertia with respect previous publications, indicating a lesser degree of differentiation.

Key Points:

- Joint analysis of the *Juno* and *Galileo* data leads to a Ganymede's degree-2 gravity compatible with hydrostatic equilibrium within $1-\sigma$
- The data hints at regional gravity anomalies with amplitudes exceeding those inferred by *Cassini* for Titan
- Treatment of non-hydrostatic effects leads to wider confidence intervals for the derived moment of inertia with respect to previous studies

Supporting Information:

Supporting Information may be found in the online version of this article.

Correspondence to:

L. Gomez Casajus,
luis.gomezcasajus@unibo.it

Citation:

Gomez Casajus, L., Ermakov, A. I., Zannoni, M., Keane, J. T., Stevenson, D., Buccino, D. R., et al. (2022). Gravity field of Ganymede after the *Juno* Extended Mission. *Geophysical Research Letters*, *49*, e2022GL099475. https://doi.org/10.1029/2022GL099475

Received 11 MAY 2022
Accepted 29 JUL 2022

1. Introduction

The *Juno* mission, dedicated to the study of the origin and evolution of Jupiter, reached the end of its Prime Mission in July 2021. After 35 orbits around Jupiter, *Juno*'s gravity experiment has succeeded on measuring the gravity field of Jupiter (Durante et al., 2020; Folkner et al., 2017; Iess et al., 2018; Serra et al., 2019), dramatically improving our knowledge on the internal tructure of the gas giant (Bolton et al., 2017), the depth of the zonal winds (Kaspi et al., 2018), the extent of internal differential rotation (Guillot et al., 2018), and more. The *Juno* Extended Mission (EM) comprises additional orbits, during which *Juno* will continue its observations of the Jupiter system. *Juno*'s highly elliptic and almost polar trajectory exploits Jupiter's oblateness perturbation to precess the periapsis of the orbit northward, allowing *Juno* to cross the satellite orbital plane during the inbound trajectory at closer distances from Jupiter during each revolution (Hansen et al., 2022). This trajectory design allowed the inclusion of 4 close encounters of the inner Galilean satellites, 1 of Ganymede, 1 of Europa and 2 of Io.

The EM trajectory started diverging from the nominal trajectory after the 32nd perijove pass (PJ32), in order to enable the first Ganymede's flyby (hereafter referred to as G34, because it occurred just before the 34th perijove pass). On 7 June 2021, *Juno* successfully performed the close encounter with Ganymede with a closest approach altitude of 1,045 km and a relative velocity of 18.5 km/s. During the flyby, a coherent two-way radio link between Juno and the antennas of the Deep Space Network (DSN) was maintained, allowing to perform a radio occultation experiment, which detected a high electron density peak during the ingress occultation consistent with an ionosphere (Buccino et al., 2022). Moreover, Doppler shift measurements were acquired, offering the opportunity to update Ganymede's gravity field for the first time since the end of the *Galileo* mission.

Planetary gravity fields are traditionally expressed in terms of spherical harmonics (e.g., Kaula, 1966; Wieczorek, 2015). The gravitational potential, U, can be written as a function of Ganymede's gravitational parameter, GM, and a set of gravitational harmonic coefficients, C_{lm} and S_{lm} as:

$$U(r,\theta,\phi) = -\frac{\mathrm{GM}}{r}\left[1 + \sum_{l=2}^{l_{\max}}\sum_{m=0}^{l}\left(\frac{R_{\mathrm{ref}}}{r}\right)^{l}\left(C_{lm}\cos m\phi + S_{lm}\sin m\phi\right)P_{lm}(\cos\theta)\right] \quad (1)$$

where r, θ, and ϕ are the radius, co-latitude and eastward longitude at the location where the potential is being evaluated, R_{ref} is the reference radius (2,631.2 km for Ganymede, not to be confused with the mean radius), P_{lm} are the unnormalized associated Legendre functions of degree l and order m, and $l_{\max}$ is the maximum degree of the model. In planetary science, it is common for the zonal coefficients (where $m = 0$) to be written as J_l, where $J_l = -C_{l0}$. Spherical harmonics of higher degree and order correspond to features at smaller wavelengths, and vice versa.

During its 8-year mission, *Galileo* performed 6 flybys of Ganymede, during which S-band Doppler data were acquired by the DSN stations. The first gravity field investigation by Anderson et al. (1996) analyzed independently the two first encounters, G1 (June 1996) and G2 (September 1996), and solved for J_2 and C_{22}. In order to further constrain the problem, Anderson et al. assumed that the ratio between the two coefficients was fixed to a value of 10/3—consistent with the assumption of a tidally-locked body in hydrostatic equilibrium (e.g., Murray & Dermott, 1999)—and they performed a weighted mean of the single arc solutions. Geophysical analysis of the gravity data as well as observations of a permanent dipole-dominant magnetic field (Kivelson et al., 2002) indicated that Ganymede is most likely differentiated into a metallic core and a silicate mantle, enclosed by an ice shell. A subsequent analysis of the gravity field, performed by Schubert et al. (2004), that added G7 (April 1997) and G29 (December 2000) to the former data set, was unable to fit the four flybys without including a degree and order 4 gravity field. Furthermore, the authors found unphysical results when the hydrostatic ratio of 10/3 for the degree-2 coefficients was not enforced. These problems could be solved with the addition of surface point mass anomalies representing smaller-scale deviations from hydrostatic equilibrium, although these point mass anomalies lacked any obvious correlation with known geologic features (Anderson et al., 2004). This point mass approach was further explored by Palguta et al. (2006, 2009). Alternatively, Jacobson et al. (2000) reported different J_2 and C_{22} coefficients, as a result of a global fit of the *Galileo* Doppler data of G1, G2, G7, and G8 (May 1997), together with an extensive data set of radiometric, spacecraft-based and ground-based astrometric observables. However, the study did not provide an internal structure interpretation.

The new measurements acquired during *Juno* G34 bring the opportunity to improve the knowledge on the gravity field of Ganymede in view of the *Europa Clipper* and *JUICE* missions, that will study the Jovian system almost simultaneously, during the 2030s.

In this paper, we present the results of a joint analysis of all the available Doppler data acquired in the vicinity of Ganymede; *Juno*'s G34 and the entire *Galileo* data set, that has been reanalyzed using modern orbit determination software and techniques adopted for the *Cassini* and *Juno* data analysis, as in Gomez Casajus et al. (2021).

2. Observation Geometry and Data

Precise orbit determination of *Juno*'s and *Galileo*'s trajectories during Ganymede's flybys allowed us to estimate Ganymede's gravity field, making use of spacecraft Doppler measurements. Those are derived from the Doppler shift of a highly stable microwave signal, induced by the relative motion between the spacecraft and the DSN stations on the Earth.

The data used in this analysis encompass the full S-band Doppler data set of *Galileo*, acquired during the 6 Ganymede's flybys: G1, G2, G7, G8, G28, and G29. The *Galileo* data set only encompasses S-band observables due to the deployment failure of its high gain antenna (HGA) (Antreasian et al., 1997), that prevented the use of the X-band. In addition, the analysis includes X- and Ka-band Doppler observables acquired during *Juno*'s G34. Table S1 in Supporting Information S1 summarizes the main characteristics of the flybys and the data used in this analysis. The ground tracks are shown in Figure 1a and Figure S1 in Supporting Information S1. Five out of seven close encounters were covered by two-way Doppler data and sampled the north-western region of Ganymede, while G8 and G28 were covered by one-way Doppler data, transmitted by the *Galileo* spacecraft

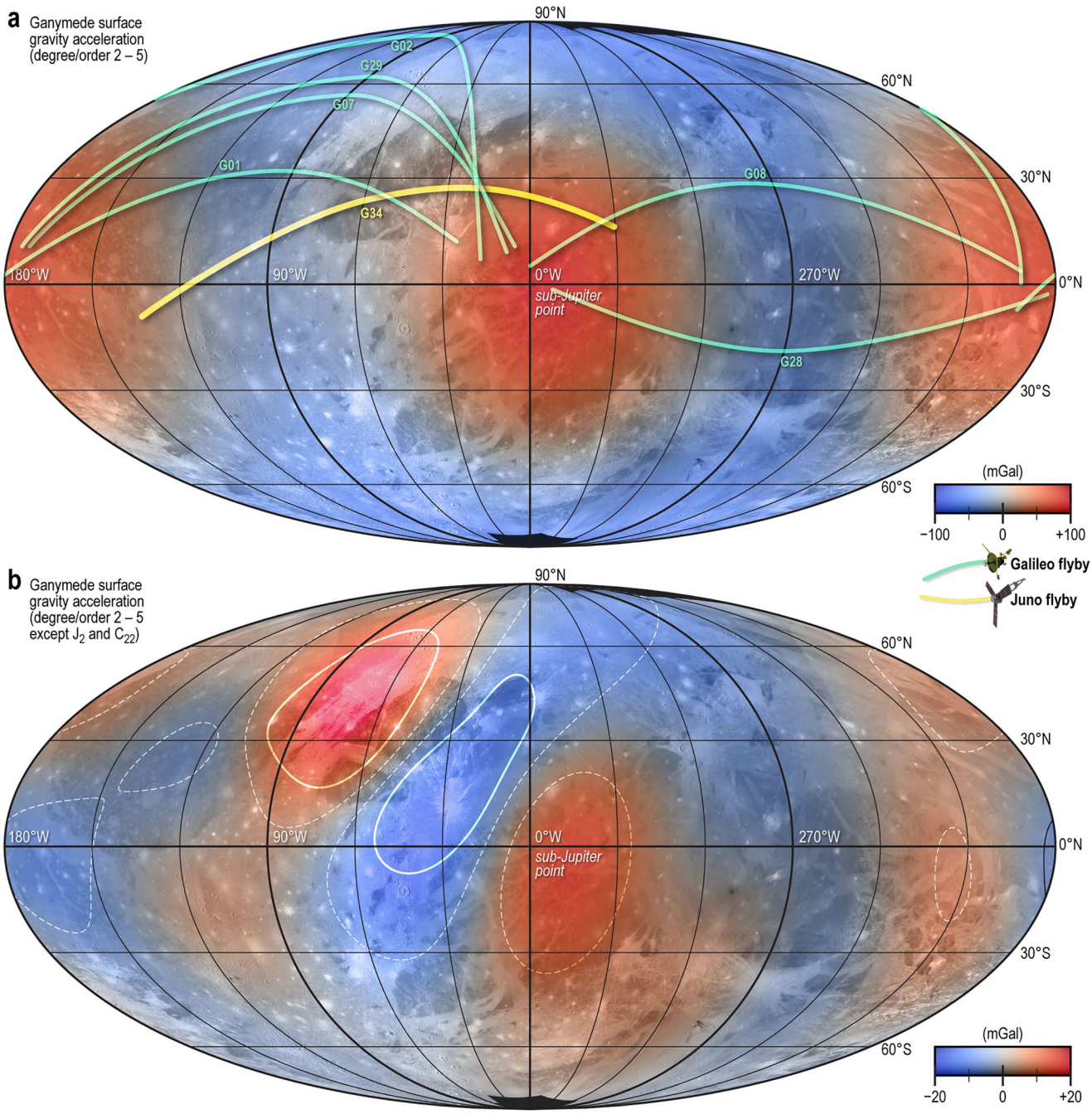

Figure 1. The gravity field of Ganymede derived from joint analysis of *Galileo* and *Juno* flyby data, computed on the reference sphere with radius 2,631.2 km. (a) The full gravity field solution, expanded to degree/order 5. Spacecraft ground tracks are shown in green (*Galileo*) and yellow (*Juno*). (b) gravity field solution, expanded to degree/order 5, removing completely the J_2 and C_{22} terms. In b, the opacity of the gravity map is scaled by the signal-to-noise ratio. The white contours enclose regions with signal-to-noise ratio greater than 1 (dashed line contour) and 3 (solid line contour). All maps are in Mollweide projection, centered on the sub-Jupiter point. Latitude and longitude grid lines are in 30° intervals. Maps are draped over a color image mosaic of Ganymede (Collins et al., 2013).

using an on-board ultra-stable oscillator, and sampled the near-equatorial eastern region. To account for possible frequency drifts on *Galileo*'s on-board clock during G8 and G28, we estimated a constant bias and a linear drift on one-way Doppler measurements.

We used Doppler data, compressed to 60 s, comprised in a 24-hr window around the closest approaches with Ganymede. Data before and after orbital maneuvers were excluded to prevent biases in the orbit determination

solution. During G34 flyby, X/Ka data were preferred over X/X observables, and two-way over three-way, in case of overlaps. Details on the data calibration can be found in Text S1 and Figure S2 in Supporting Information S1.

The data were weighted on a pass-by-pass basis using the root mean square of the residuals. Additionally, G29 data were de-weighted to take into account possible Io Plasma Torus (e.g., Bagenal, 1994; Moirano et al., 2021) calibration errors. Finally, the one-way passes were de-weighted by a factor of 2, to take into account the poorer stability of the non-coherent link.

3. Methods

The data analysis is based on the heritage of the *Cassini* and *Juno* radio science analyses (Durante et al., 2019; Tortora et al., 2016; Zannoni et al., 2020) and it has been performed with the latest JPL's orbit determination program, MONTE (Evans et al., 2018). The data have been fitted using a Batch Weighted Least Squares Filter (Bierman, 2006) to iteratively update an a priori dynamical model. The dynamical model included all the relevant forces that contributed to the motion of *Galileo*, *Juno* and Ganymede during the 7 close encounters. Hence, the model included the relativistic point mass acceleration due to all the relevant bodies of the Solar System, that is, the Sun, the planets and the Jovian satellites. The gravity field of Jupiter and its satellites was included, and modeled by means of their standard spherical harmonic representation (Durante et al., 2020; Schubert et al., 2004). For Ganymede, we adopted a dynamically defined, perfectly synchronous frame, in which the x-axis points to the average empty focus of the orbit, with zero-obliquity. Other frames were used to check the stability of the solution, providing fully consistent results (Archinal et al., 2018). For Jupiter, instead, we used the rotational model included in JPL's reference ephemeris JUP365. The dynamical model also included the solar radiation pressure acting on both *Galileo* and *Juno*. Other non-gravitational accelerations were neglected in the nominal dynamical model, but were included separately to assess the stability of the solution: the non-isotropic thermal emission due to *Galileo*'s radioisotope thermoelectric generators and the atmospheric drag due to the tenuous neutral atmosphere of Ganymede (Leblanc et al., 2017).

The data have been fitted using a multi-arc approach (Milani & Gronchi, 2010) in which the Doppler data acquired during different encounters, called arcs, are jointly analyzed to estimate a set of global parameters that are constant for all the encounters, and local parameters that influence the single arcs.

Our global parameters encompass the gravity field of Ganymede, represented by a linear combination of spherical harmonics functions (Equation 1), parameterized by its gravitational parameter GM and the gravitational harmonic coefficients, C_{lm} and S_{lm} up to degree and order 5. The a priori uncertainties on the degree-2 coefficients were large enough to not constrain the solution. Unlike Anderson et al. (1996), no a priori equilibrium condition was imposed between J_2 and C_{22}. Since a gravity model of degree and order larger than 2 was needed to fit the data and the spatial coverage of the flybys was limited (see Figure S1 in Supporting Information S1), we needed to include an a priori constraint on the normalized coefficients on degrees $l > 2$ following Kaula's rule AK/l^2(Kaula, 1963). The nominal coefficient $K = 0.9 \times 10^{-5}$ was obtained scaling the corresponding value estimated for Titan (Durante et al., 2019) to Ganymede (Bills et al., 2014), while the scale factor $A = 4$ was retrieved finding the minimum power of the field that allowed us to fit the data satisfactorily. (More details on the method can be found in Text S2 and Figures S3–S6 in Supporting Information S1). The factor A approximately corresponds to how much more non-hydrostatic power compared to Titan was required to satisfactorily explain the *Galileo* and *Juno* Doppler data at Ganymede.

The set of local parameters include the state of *Galileo* and *Juno* at the beginning of each arc. The initial values were retrieved from the latest available trajectories reconstructed by the navigation teams, with an a priori uncertainty large enough to not constrain the solution. Since the reconstruction of a coherent orbit of Ganymede around Jupiter was beyond the scope of this work, the orbit of Ganymede was treated as a local parameter, estimating an updated state vector at the beginning of each arc. In fact, in the analysis we only used the data acquired during the Ganymede flybys of *Galileo* and *Juno*, separated by more than 20 years. Moreover, the Jovian system is subject to complex dynamics, as the Laplace resonance and tidal interactions (e.g., Lari et al., 2020). The local strategy allows to overcome the difficulties of a global, fully consistent, fit of the orbit, conservatively increasing the obtained uncertainties. Finally, local parameters include: a scale factor for the solar radiation pressure acceleration, Doppler biases for three-way passes, and Doppler biases and linear drifts for the one-way passes.

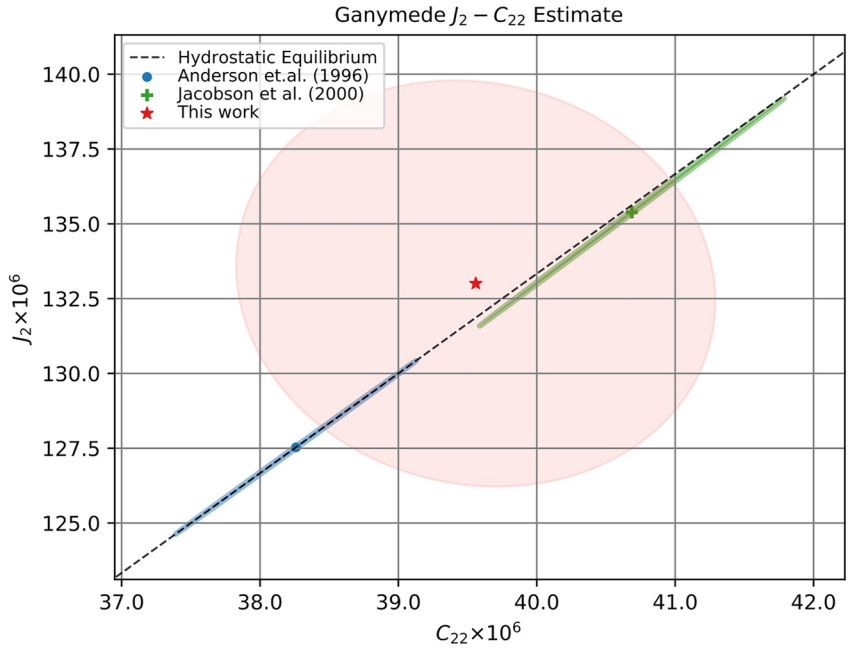

Figure 2. Obtained J_2 and C_{22} and its $1-\sigma$ associated uncertainty (red ellipse). In addition, the figure shows both the solutions of Anderson et al. (1996) and Jacobson et al. (2000) as blue and green lines, respectively.

Due to the low eccentricity of Ganymede's orbit and the limited sampling of mean anomaly during the different flybys of Ganymede (see Table S1 in Supporting Information S1) the tidal Love number k_2 could not be estimated. Moreover, the rotational parameters of Ganymede were not estimated due to the low sensitivity of data.

4. Gravity Field Results

Figure 1a shows the full, best-fit gravity field of Ganymede. The predominant pattern in this gravity field is the long-wavelength, degree-2 pattern represented by J_2 and C_{22} arising from the tidal and rotational forces acting on Ganymede. However, similarly to Anderson et al. (2004) and Schubert et al. (2004) a pure degree-2 gravity field was not sufficient to fit the data to the noise level. Signatures in the residuals arise due to the low-altitude *Galileo* flybys G1 and G2, which increase the sensitivity to the higher degrees. We were able to fit the data to the noise level using a gravity field solution with a minimum degree and order 5. The obtained residuals can be found in Figures S5 and S6 in Supporting Information S1. Figure 2 shows the estimated values of J_2 and C_{22} in the C_{22}-J_2 plane. Our degree-2 gravity field (red ellipse) is compatible with a body in hydrostatic equilibrium (black dashed line) within $1-\sigma$. The coefficients differ by about $1-\sigma$ from the values estimated by Anderson et al. (1996), while remain compatible with Jacobson et al. (2000) within $1-\sigma$. As reference, all the estimated gravity field coefficients are reported in Table S2 in Supporting Information S1.

We would like to point out that, even though we performed a joint analysis of *Galileo* and *Juno* data, the obtained formal uncertainties are larger than the ones present in literature. These differences may come from a number of reasons. For example, Anderson et al. (1996) only estimated two gravity coefficients, J_2 and C_{22}, applying the hydrostatic equilibrium constraint, effectively reducing the number of gravity-related parameters to one, and therefore obtaining overly optimistic results. Another source of discrepancy may come from the ephemerides treatment: in our analysis we updated the ephemerides during each arc, while Jacobson et al. (2000) used a global fit of all the Galilean satellites for the entire timespan of the observations, and Anderson et al. (1996) did not update them.

Most of the individual estimated coefficients at $l > 2$ are compatible with zero and carry little meaning by themselves. However, they have a clear effect on the surface gravity. While the presence of a higher degree and order gravity field can be seen in Figure 1a, it can be more clearly highlighted by removing the J_2 and C_{22} terms, which are primarily (although not entirely) driven by tidal and rotational deformation, which is illustrated in

Figure 1b. Figure 1b evidences two different localized gravity anomalies with amplitudes larger than 3 times the retrieved formal uncertainty, one positive, centered at 72°W, 43°N, with an amplitude of 23 mGal ± 11.7 (3−σ), and another negative with the peak at 40°W, 1°S, with an a amplitude of −17.9 mGal ± 14.0 (3−σ). Figure 1b does not include the gravity anomalies due to the unknown non-hydrostatic contribution to J_2 and C_{22}. Assuming the same non-hydrostaticity level of Titan (Durante et al., 2019) rescaled to Ganymede, the degree-2 contribution corresponds to a surface value of ∼1 mGal. If we consider a value four times larger it corresponds to ∼4 mGal, still significantly smaller than the observed $l > 2$ anomalies. Due to the limited spatial coverage of the flybys, all the statistically significative gravity anomalies are located in the north-western region of Ganymede, in correspondence of the ground tracks. The positive gravity region covers the old light subdued material (unit is_1 in Collins et al., 2013) surrounding Xibalba Sulcus. The negative gravity anomaly region is centered at the Tros crater. Stereographic observations of Tros crater were acquired during the *Juno* flyby (Ravine et al., 2022).

The presence of this higher degree gravity signal indicates that geologic phenomena could be contributing to the observed gravity field (Figure 1b). This was previously suggested with point mass-based models by Anderson et al. (2004) and Palguta et al. (2006, 2009). Palguta et al. (2009) hypothesized that Ganymede's dark terrains were correlated with positive gravity anomalies (red in Figure 1b), and that Ganymede's bright terrains were correlated with negative gravity anomalies (blue in Figure 1b). At first glance, this correlation may hold with our new gravity field, although a detailed analysis of this higher degree and order gravity field (including the large uncertainties therein) are left for future work. Finally, we note that given the lack of Ganymede shape data, it is impossible to uniquely attribute the observed anomalies to surface observations. For ocean worlds, the observed gravity anomalies can be sourced from deeper interfaces with associated density contrasts, such as ice-ocean and ocean-rocky core interfaces as was previously hypothesized for Europa (Dombard & Sessa, 2019; Pauer et al., 2010).

In our analysis localized non-hydrostatic features with amplitudes higher than those found on Titan by the *Cassini* mission are identified. Titan is a useful comparison case as it shares with Ganymede nearly the same mean radius, mean density, and therefore, surface gravity. Thus, the non-hydrostatic deviations of the same amplitude either in shape or in gravity would correspond to approximately the same level of non-hydrostatic stress. On Titan, the gravity field for $l > 2$ reaches at most 5 mGal (Durante et al., 2019), which is a factor of 5 smaller than the largest anomalies we recovered on Ganymede. One key difference between the two bodies is the lack of atmosphere-based erosion processes on Ganymede. Such erosional processes could have led to faster removal of non-hydrostatic signals at Titan reducing the amplitude of its gravity anomalies. In addition, Titan's outer shell could be thinner and, therefore, less rigid than that of Ganymede, thus not being able to support as much non-hydrostaticity. However, we note that the gravity field of Titan has a better global characterization, because of the better spatial coverage and data quality provided by the *Cassini* spacecraft. When compared to Titan, our current knowledge of Ganymede is still limited. Further insights into Ganymede internal structure will be coming from the *JUICE* mission on the next decade.

5. Implications on the Internal Structure

Previous works that enforced the hydrostatic ratio of 10/3 for J_2/C_{22} (e.g., Anderson et al., 1996) derived Ganymede's moment of inertia (MOI) using the Radau-Darwin relationship. However, this approach introduces two sources of error in the recovered value. First, the Radau-Darwin relationship can be applied only to a body in hydrostatic equilibrium. The real Ganymede has some non-hydrostaticity as indicated by the higher degree observed gravity. Second, the Radau-Darwin relationship is itself an approximation. That is, even for a body in hydrostatic equilibrium, there is not a one-to-one correspondence between the second degree gravity coefficients and the MOI. To eliminate these two sources of uncertainty in the internal structure modeling, we used a Markov chain Monte-Carlo (MCMC) approach. We built a three constant-density layer model of Ganymede satisfying Ganymede's mass and radius (see Text S3 and Table S3 in Supporting Information S1). We ran the MCMC using the affine invariant ensemble sampler (Foreman-Mackey et al., 2013; Goodman & Weare, 2010) with the log-likelihood function $\ln(L) = -\frac{1}{2}(X-Y)^T \Sigma^{-1}(X-Y)$, where X is the vector of synthetic observables, Y is the vector of observed values of the gravity coefficients, and Σ their covariance matrix. The model values X consisted of the hydrostatic and non-hydrostatic parts: $\left\{C_{20}^h + C_{20}^{nh}\left(\sigma_2^{nh}\right), C_{22}^h + C_{22}^{nh}\left(\sigma_2^{nh}\right)\right\}$. At each step in the chain, the non-hydrostatic parts were sampled from the normal distribution with a standard deviation of σ_2^{nh}.

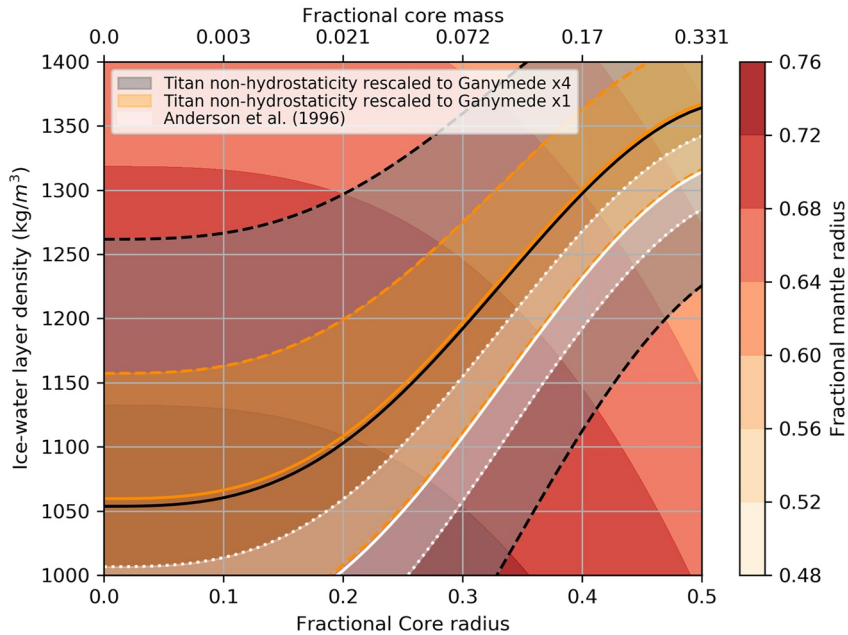

Figure 3. Three-layer models of Ganymede satisfying the measured total mass, total radius, and the different computed moments of inertia. We assumed an iron core density of 5,500 kg/m^3 and a mantle density of 3,300 kg/m^3. The gray and orange areas show the possible models compatible with our solutions considering different degrees of non-hydrostaticity contribution on the degree 2, while the white one represents Anderson et al. (1996) results. The contours show the fractional rock-mantle radius compatible with the total mass and radius. The upper scale for the fractional core mass is non-linear.

The hydrostatic parts were computed using the second order in eccentricity method from Tricarico (2014). We derived the confidence intervals for the MOI from the Markov chains for a range of σ_2^{nh}. In the limiting case of zero non-hydrostaticity, we derived a MOI of $0.3161^{+0.0040}_{-0.0040}$, where the lower and upper bounds correspond to 16th and 84th percentile, respectively. Here we report moments of inertia for an interior model with volume-equivalent spherical layers. Assuming non-hydrostaticity based on Titan's observed gravity power law (Durante et al., 2019) rescaled to Ganymede ($\sigma_2^{nh} = 2.25 \times 10^{-6}$), we obtained a MOI of $0.3159^{+0.0052}_{-0.0052}$. Finally, for non-hydrostaticity 4 times larger than the one of Titan, which is motivated by the observed amplitude of gravity anomalies, we derived a MOI of $0.3156^{+0.0117}_{-0.0133}$. The MOI confidence intervals for a range of σ_2^{nh} are shown in Figure S7 in Supporting Information S1. The inferred normalized MOIs correspond to a slightly less differentiated interior structure than Anderson et al. (1996) of 0.3105 ± 0.0028. With the same MCMC procedure, we derived the expected hydrostatic semiaxes differences of $a - c = 1.84^{+0.03}_{-0.03}$ km and $a - b = 1.38^{+0.02}_{-0.02}$ km, where a is the longest axis directed toward Jupiter, c is the shortest polar axis and b is the intermediate axis, taking the volumetric radius of 2,632.70 km that corresponds to Ellipsoid I from Zubarev et al. (2015). The error bars increased to 0.6 and 0.8 km for $a - c$ and $a - b$, respectively, for a non-hydrostaticity 4 times that of Titan.

We used the derived MOI in combination with the mass and radius of Ganymede to place constraints on its internal structure. We followed the approach taken by Anderson et al. (1996) to allow for a direct comparison. We adopted a three-layer model consisting of a metallic core of Fe-FeS with a density of 5,150 kg/m^3, a silicate mantle with a density of 3,300 kg/m^3, and an ice-water layer with a density in the range of 1,000–1,400 kg/m^3. The thickness of the hydrosphere was computed to match Ganymede's mass for a given core radius and outer layer density. This approach has the merit of avoiding compositional assumptions for the outer region (ice and water dominated) and does not apply any cosmochemical or phase relationship constraints on it. Figure 3 shows all possible Ganymede models that, under those assumptions, satisfy the measured values of total mass, total radius, and the MOI. This simplified analysis yields a core radius that ranges up to ~50% of the total radius, representing up to the 33% of Ganymede's mass. The core radius cannot exceed this value without the complete disappearance of the mantle. Similarly, the ice-water density of the possible models ranges from ~1,060 kg/m^3 up to ~1,370 kg/m^3. For convenience, Figure 3 shows also the models that are compatible with the results from Anderson et al. (1996). Given the retrieved MOI, for the same core radius our models require a denser ice-water layer. However, the larger derived uncertainties allow for a larger variation in the densities of the internal layers

as compared to Anderson et al. (1996). Thus, non-hydrostaticity limits the ability to recover the MOI and internal structure.

Currently, there is not a global shape model of Ganymede with the accuracy sufficient for geophysical analysis. The lack of an accurate shape model prevented us from separating degree-2 hydrostatic from non-hydrostatic contributions. More complex models could be produced, but they would require additional assumptions and other data sets and are left for future work.

6. Conclusions

We analyzed the Doppler data acquired by the DSN stations during the latest Ganymede encounter of *Juno*, together with the *Galileo* data, to update the gravity field model of the largest moon of the Solar system. We obtained a satisfactory fit of the data estimating a full field of degree and order 5 without imposing the hydrostatic equilibrium constraint between J_2 and the C_{22}. This gravity field confirms the detection of local gravity anomalies at shorter wavelength (degree 3 to 5), first suggested by *Galileo* data (Anderson et al., 2004; Palguta et al., 2006, 2009). These shorter wavelength gravity anomalies, with amplitudes larger than the ones found in Titan (Durante et al., 2019), may trace either shallow geologic phenomena or could arise due to deep-seated phenomena such as non-hydrostatic interfaces associated with density contrasts (e.g., ice-rock or ice-ocean boundaries). The derived moment of inertia corresponds to a slightly less differentiated interior structure than previous analyses. However, taking into account the observed non-hydrostaticity leads to a larger, but more realistic, uncertainty in the moment of inertia.

The data used in this analysis will be the last gravity measurements of Ganymede until future Ganymede flybys by the ESA *JUICE* and NASA *Europa Clipper* missions in the next decade.

Data Availability Statement

The *Juno* radio science data used in this research are publicly available through NASA's Planetary Data System at https://atmos.nmsu.edu/PDS/data/jnogrv_1001/ (D. R. Buccino, 2016). *Galileo* tracking data are publicly available through NASA's Planetary Data System https://pds-ppi.igpp.ucla.edu/mission/Galileo/GO/RSS. The gravity field presented here is provided in a corresponding data set with this publication on Zenodo (Gomez Casajus et al., 2022).

Acknowledgments
The authors are grateful to William Folkner, to the entire Solar System Dynamics Group and to Robert Haw, former *Galileo* navigator, for the useful discussions and suggestions regarding the procedures for *Galileo* data analysis. L.G.C., M.Z., and P.T. are grateful to the Italian Space Agency (ASI) for financial support through Agreement No. 2017-40-H.1-2020, and its extension 2017-40-H.02020-13-HH.0, for ESA's BepiColombo and NASA's *Juno* radio science experiments. L.G.C., M.Z., and P.T. acknowledge Caltech and the Jet Propulsion Laboratory for granting the University of Bologna a license to an executable version of MONTE Project Edition S/W. JTK and AIE acknowledge support from the *Juno* participating scientist program. The work of RP, DB, JTK, and MP was carried out at the Jet Propulsion Lab, California Institute of Technology, under a contract with the National Aeronautics and Space Administration (80NM0018D0004). Government sponsorship acknowledged.

References

Anderson, J. D., Lau, E. L., Sjogren, W. L., Schubert, G., & Moore, W. B. (1996). Gravitational constraints on the internal structure of Ganymede. *Nature*, *384*(6609), 541–543. https://doi.org/10.1038/384541a0

Anderson, J. D., Schubert, G., Jacobson, R. A., Lau, E. L., Moore, W. B., & Palguta, J. L. (2004). Discovery of mass anomalies on Ganymede. *Science*, *305*(5686), 989–991. https://doi.org/10.1126/science.1099050

Antreasian, P. G., McElrath, T. P., Haw, R. J., Lewis, G. D., & Krisher, T. (1997). Galileo orbit determination results during the satellite tour.

Archinal, B. A., Acton, C. H., A'Hearn, M. F., Conrad, A., Consolmagno, G. J., Duxbury, T., et al. (2018). Report of the IAU working Group on Cartographic coordinates and rotational elements: 2015. *Celestial Mechanics and Dynamical Astronomy*, *130*(3), 22. https://doi.org/10.1007/s10569-017-9805-5

Bagenal, F. (1994). Empirical model of the Io plasma torus: Voyager measurements. *Journal of Geophysical Research*, *99*(A6), 11043–11062. https://doi.org/10.1029/93JA02908

Bierman, G. J. (2006). *Factorization methods for discrete sequential estimation*. Courier Corporation.

Bills, B. G., Asmar, S. W., Konopliv, A. S., Park, R. S., & Raymond, C. A. (2014). Harmonic and statistical analyses of the gravity and topography of Vesta. *Icarus*, *240*, 161–173. https://doi.org/10.1016/j.icarus.2014.05.033

Bolton, S. J., Adriani, A., Adumitroaie, V., Allison, M., Anderson, J., Atreya, S., et al. (2017). Jupiter's interior and deep atmosphere: The initial pole-to-pole passes with the Juno spacecraft. *Science*, *356*(6340), 821–825. https://doi.org/10.1126/science.aal2108

Buccino, D. R. (2016). Juno Jupiter gravity science raw data set V1.0, JUNO-J-RSS-1 JUGR-V1.0, NASA planetary data system (PDS). Retrieved from https://atmos.nmsu.edu/PDS/data/jnogrv_1001/

Buccino, D. R., Parisi, M., Gramigna, E., Gomez-Casajus, L., Tortora, P., Zannoni, M., et al. (2022). Ganymede's ionosphere observed by a dual-frequency radio occultation with Juno. *Geophysical Research Letters*, *49*, e2022GL098420. https://doi.org/10.1029/2022gl098420

Collins, G. C., Patterson, G. W., Head, J. W., Pappalardo, R. T., Prockter, L. M., Lucchitta, B. K., & Kay, J. P. (2013). Global geologic map of Ganymede: U.S. Geological Survey Scientific investigations map 3237, pamphlet 4 p., 1 sheet, scale 1:15,000,000. https://doi.org/10.3133/sim3237

Dombard, A. J., & Sessa, A. M. (2019). Gravity measurements are key in addressing the habitability of a subsurface ocean in Jupiter's Moon Europa. *Icarus*, *325*, 31–38. https://doi.org/10.1016/j.icarus.2019.02.025

Durante, D., Hemingway, D. J., Racioppa, P., Iess, L., & Stevenson, D. J. (2019). Titan's gravity field and interior structure after Cassini. *Icarus*, *326*, 123–132. https://doi.org/10.1016/j.icarus.2019.03.003

Durante, D., Parisi, M., Serra, D., Zannoni, M., Notaro, V., Racioppa, P., et al. (2020). Jupiter's gravity field halfway through the Juno mission. *Geophysical Research Letters*, *47*(4), e2019GL086572. https://doi.org/10.1029/2019GL086572
Evans, S., Taber, W., Drain, T., Smith, J., Wu, H., Guevara, et al. (2018). MONTE: The next generation of mission design and navigation software. *CEAS Space Journal*, *10*, 79–86. https://doi.org/10.1007/s12567-017-0171-7
Folkner, W. M., Iess, L., Anderson, J. D., Asmar, S. W., Buccino, D. R., Durante, D., et al. (2017). Jupiter gravity field estimated from the first two Juno orbits. *Geophysical Research Letters*, *44*(10), 4694–4700. https://doi.org/10.1002/2017GL073140
Foreman-Mackey, D., Hogg, D. W., Lang, D., & Goodman, J. (2013). emcee: The MCMC hammer. *Publications of the Astronomical Society of the Pacific*, *125*(925), 306–312. https://doi.org/10.1086/670067
Gomez Casajus, L., Ermakov, A. I., Zannoni, M., Keane, J. T., Stevenson, D., Buccino, D. R., et al. (2022). Corresponding dataset for gravity field of Ganymede after the Juno Extended Mission (v1.0) [Dataset]. Zenodo. https://doi.org/10.5281/zenodo.6949645
Gomez Casajus, L., Zannoni, M., Modenini, D., Tortora, P., Nimmo, F., Van Hoolst, T., et al. (2021). Updated Europa gravity field and interior structure from a reanalysis of Galileo tracking data. *Icarus*, *358*, 114187. https://doi.org/10.1016/j.icarus.2020.114187
Goodman, J., & Weare, J. (2010). Ensemble samplers with affine invariance. *Communications in Applied Mathematics and Computational Science*, *5*(1), 65–80. https://doi.org/10.2140/camcos.2010.5.65
Guillot, T., Miguel, Y., Militzer, B., Hubbard, W. B., Galanti, E., Kaspi, Y., et al. (2018). A suppression of differential rotation in Jupiter's deep interior. *Nature*, *555*(7695), 227–230. https://doi.org/10.1038/nature25775
Hansen, C. J., Bolton, S., Brennan, M., Lunine, J., Sulaiman, A., Levin, S., et al. (2022). Overview of Juno's flyby of Ganymede. *Geophysical Research Letters*, *49*, e2022GL099285. https://doi.org/10.1029/2022GL099285
Iess, L., Folkner, W. M., Durante, D., Parisi, M., Kaspi, Y., Galanti, E., et al. (2018). The measurement of Jupiter's asymmetric gravity field. *Nature*, *555*(7695), 220–222. https://doi.org/10.1038/nature25776
Jacobson, R. A., Haw, R. J., McElrath, T. P., & Antreasian, P. G. (2000). A comprehensive orbit reconstruction for the Galileo prime mission in the J2000 system. *Journal of the Astronautical Sciences*, *48*(4), 495–516. https://doi.org/10.1007/BF03546268
Kaspi, Y., Galanti, E., Hubbard, W. B., Stevenson, D. J., Iess, L., Guillot, T., et al. (2018). The extension of Jupiter's jet to a depth of thousands of kilometers. *Nature*, *555*(7695), 223–226. https://doi.org/10.1038/nature25793
Kaula, W. M. (1963). Determination of the Earth's gravitational field. *Review of Geophysics*, *1*(4), 507. https://doi.org/10.1029/RG001i004p00507
Kaula, W. M. (1966). *Introduction to satellite Geodesy, chap. 1* (pp. 1–11). Blaisdell.
Kivelson, M. G., Khurana, K. K., & Volwerk, M. (2002). The permanent and inductive magnetic moments of Ganymede. *Icarus*, *157*(2), 507–522. https://doi.org/10.1006/icar.2002.6834
Lari, G., Saillenfest, M., & Fenucci, M. (2020). Long-term evolution of the Galilean satellites: The capture of Callisto into resonance. *Astronomy & Astrophysics*, *639*, A40. https://doi.org/10.1051/0004-6361/202037445
Leblanc, F., Oza, A. V., Leclercq, L., Schmidt, C., Cassidy, T., Modolo, R., et al. (2017). On the orbital variability of Ganymede's atmosphere. *Icarus*, *293*, 185–198. https://doi.org/10.1016/j.icarus.2017.04.025
Milani, A., & Gronchi, G. (2010). *Theory of orbit determination*. Cambridge University Press. https://doi.org/10.1017/CBO9781139175371
Moirano, A., Gomez Casajus, L., Zannoni, M., Durante, D., & Tortora, P. (2021). Morphology of the Io Plasma Torus from Juno radio occultations. *Journal of Geophysical Research: Space Physics*, *126*(10), e2021JA029190. https://doi.org/10.1029/2021JA029190
Murray, C. D., & Dermott, S. F. (1999). *Solar system dynamics*. Cambridge university press. https://doi.org/10.1017/CBO9781139174817
Palguta, J., Anderson, J. D., Schubert, G., & Moore, W. B. (2006). Mass anomalies on Ganymede. *Icarus*, *180*(2), 428–441. https://doi.org/10.1016/j.icarus.2005.08.020
Palguta, J., Schubert, G., Zhang, K., & Anderson, J. D. (2009). Constraints on the location, magnitude, and dimensions of Ganymede's mass anomalies. *Icarus*, *201*(2), 615–625. https://doi.org/10.1016/j.icarus.2009.02.004
Pauer, M., Musiol, S., & Breuer, D. (2010). Gravity signals on Europa from silicate shell density variations. *Journal of Geophysical Research*, *115*(E12), E12005. https://doi.org/10.1029/2010JE003595
Ravine, M. A., Hansen, C. J., Collins, G. C., Schenk, M. A., Caplinger, M. A., Lipkaman Vittling, L., et al. (2022). Ganymede observations by JunoCam on Juno Perijove 34. *Geophysical Research Letters*, *49*, e2022GL099211. https://doi.org/10.1029/2022GL099211
Schubert, G., Anderson, J. D., Spohn, T., & McKinnon, W. B. (2004). Interior composition, structure and dynamics of the Galilean satellites. *Jupiter: The planet, satellites and magnetosphere*, *1*, 281–306.
Serra, D., Lari, G., Tommei, G., Durante, D., Gomez Casajus, L., Notaro, V., et al. (2019). A solution of Jupiter's gravitational field from Juno data with the ORBIT14 software. *Monthly Notices of the Royal Astronomical Society*, *490*(1), 766–772. https://doi.org/10.1016/10.1093/mnras/stz2657
Tortora, P., Zannoni, M., Hemingway, D., Nimmo, F., Jacobson, R. A., Iess, L., & Parisi, M. (2016). Rhea gravity field and interior modeling from Cassini data analysis. *Icarus*, *264*, 264–273. https://doi.org/10.1016/j.icarus.2015.09.022
Tricarico, P. (2014). Multi-layer hydrostatic equilibrium of planets and synchronous moons: Theory and application to Ceres and to Solar System Moons. *The Astrophysical Journal*, *782*(2), 99. https://doi.org/10.1088/0004-637x/782/2/99
Wieczorek, M. A. (2015). Gravity and topography of the terrestrial Planets. In *Treatise on geophysics* (pp. 153–193). https://doi.org/10.1016/B978-0-444-53802-4.00169-X
Zannoni, M., Hemingway, D., Casajus, L. G., & Tortora, P. (2020). The gravity field and interior structure of Dione. *Icarus*, *345*, 113713. https://doi.org/10.1016/j.icarus.2020.113713
Zubarev, A., Nadezhdina, I., Oberst, J., Hussmann, H., & Stark, A. (2015). New Ganymede control point network and global shape model. *Planetary and Space Science*, *117*, 246–249. https://doi.org/10.1016/j.pss.2015.06.022

References From the Supporting Information

Bar-Sever, Y. E., Jacobs, C. S., Keihm, S., Lanyi, G. E., Naudet, C. J., Rosenberger, H. W., et al. (2007). Atmospheric media calibration for the deep space network. *Proceedings of the IEEE*, *95*(11), 2180–2192. https://doi.org/10.1109/JPROC.2007.905181
Bertotti, B., Comoretto, G., & Iess, L. (1993). Doppler tracking of spacecraft with multi-frequency links. *Astronomy and Astrophysics*, *269*, 608–616.

Estefan, J. A., & Sovers, O. J. (1994). A comparative Survey of current and proposed tropospheric refraction-delay models for DSN radio metric data calibration.

Mariotti, G., & Tortora, P. (2013). Experimental validation of a dual uplink multifrequency dispersive noise calibration scheme for deep space tracking. *Radio Science*, *48*(2), 111–117. https://doi.org/10.1002/rds.20024

Phipps, P. H., Withers, P., Buccino, D. R., & Yang, Y. M. (2018). Distribution of plasma in the Io plasma torus as seen by radio occultation during Juno Perijove 1. *Journal of Geophysical Research: Space Physics*, *123*(8), 6207–6222. https://doi.org/10.1029/2017JA025113